Nanoscale Advances

ROYAL SOCIETY OF CHEMISTRY

PAPER

Cite this: *Nanoscale Adv.*, 2022, **4**, 1414

Hollow carbon nanospheres embedded with stoichiometric γ-Fe_2O_3 and $GdPO_4$: tuning the nanospheres for *in vitro* and *in vivo* size effect evaluation†

Hui Zhang,‡[a] Jianping Zhang,‡[b] Yi Chen,[a] Tianze Wu,[a] Mingzhu Lu,[a] Zhenxia Chen,[a] Yu Jia,[a] Yongtai Yang,[a] Yun Ling *[ac] and Yaming Zhou *[a]

The size modulation of hollow carbon nanospheres (HCSs) has attracted great interest in the contexts of cellular uptake, drug delivery and bioimaging. In this study, a facile fabrication method was specifically used to minimize all influencing factors except for the particle size. A series of nanoparticles of hollow carbon nanospheres embedded with magnetic resonance imaging (MRI) nanoagent γ-Fe_2O_3 and $GdPO_4$ nanoparticles (Fe–Gd/HCS), were successfully prepared and applied to *in vitro*/*vivo* evaluation with well-defined sizes of ~100 nm (Fe–Gd/HCS-S), ~200 nm (Fe–Gd/HCS-M), and ~300 nm (Fe–Gd/HCS-L), respectively. Then the *in vitro* size effect of Fe–Gd/HCS was systematically investigated by bio-TEM, CLSM, CCK-8 assay, and flow cytometry revealing that Fe–Gd/HCS could be internalized and the cellular uptake amounts increase with the decrease of size. Furthermore, the *in vivo* size-effect behavior of Fe–Gd/HCS (~100 nm, ~200 nm, ~300 nm) was tracked by MRI technique, demonstrating that all Fe–Gd/HCS can distinguish the liver, in which Fe–Gd/HCS with the smallest particle size exhibited the best performance among these nanoparticles. By leveraging on these features, Fe–Gd/HCS-S (~100 nm) was further chosen as a theranostic agent, preliminarily presenting its capability for multi-modal imaging and therapy.

Received 25th October 2021
Accepted 19th January 2022

DOI: 10.1039/d1na00771h

rsc.li/nanoscale-advances

Introduction

Hollow nanospheres have become increasingly attractive for application in micro-/nano-reactors,[1–4] catalysis,[5,6] energy storage,[7–10] and biomedicine[11–14] due to their unique hollow nanostructure, tunable size/thickness, large surface area, low density and high loading capacity. Currently, the composition of hollow spherical shells has also evolved from silica and polymers, resulting in much more functional materials such as metals, metal oxides, and complex compounds. Based on the hollow spherical shell, these materials have been applied in various fields, especially in biomedicine.[15,16] Hollow carbon nanospheres (HCSs), one of the hollow nanospheres with shell composition of carbon, have been widely used as biosensors, drug carriers, and photothermal agents owing to the combination of a hollow nanostructure, intrinsic carbon properties and excellent biocompatibility.[17–20] In these biomedical applications, the introduction of HCSs into biological fluids and tissues is required, which frequently depends on the internalization of these nanoparticles by cells.[21–24] Therefore, it is imperative to investigate the biological behaviors of HCSs in order to explore and optimize the biomedical applications of HCSs.

Generally, the extent and efficiency of the cellular uptake of nanoparticles strongly depend on the particle size, morphology, surface charge, and surface chemistry.[24–29] In recent years, studies have found that the size plays a critical role in modulating interactions between nanoparticles and biological systems. Thus it is of significance to study the size effect to achieve high therapeutic efficiency.[30–32] It has been reported that different-size nanoparticles may enter cells *via* different internalization pathways, or even multiple pathways. And nanoparticles with suitable size can directly contribute to faster adherence to cells and higher efficiency of cellular uptake. However, previous studies of HCS nanoparticles usually focused on the properties of drug delivery and imaging, but the investigation of the size effect on cellular uptake, cytotoxicity, and *in vivo* behavior has not been specifically explored and evaluated. On the other hand, the complexity of *in vivo* systems and

[a]*Shanghai Key Laboratory of Molecular Catalysis and Innovative Materials, Department of Chemistry, Fudan University, Shanghai, 200433, China. E-mail: yunling@fudan.edu.cn; ymzhou@fudan.edu.cn*

[b]*Department of Nuclear Medicine, Fudan University Shanghai Cancer Center, Shanghai, 200032, China*

[c]*Zhuhai Fudan Innovation Institute, Zhuhai, Guangdong, 519000, China*

† Electronic supplementary information (ESI) available. See DOI: 10.1039/d1na00771h

‡ These two authors contributed equally to this work.

inherent inertness of carbon also limit the assessment and understanding of the *in vivo* size effect. Therefore, using appropriate techniques to explore the *in vivo* size effect of HCSs is urgent, which could further optimize the diagnostic sensitivity and therapeutic efficacy. Magnetic resonance imaging (MRI), one of the best noninvasive and highly sensitive methodologies for clinical diagnostics, was chosen to be applied to test the performances of HCSs *in vivo*.[33,34] Our groups previously developed a serial of functionalized magnetic carbon materials using post-synthetic modification with Wells–Dawson-like heterometallic clusters $\{Fe_6Gd_6P_6\}$, which possessed T_1 and T_2 MRI enhanced capabilities.[35,36] In this context, MRI nanoagents of γ-Fe_2O_3 and $GdPO_4$ nanoparticles were embedded into HCSs making it feasible to evaluate the size effect *in vivo* by MRI tracking.

Herein, three hollow carbon nanospheres of different sizes (~100 nm, ~200 nm, and ~300 nm) embedded with magnetic nanoparticles of γ-Fe_2O_3 and $GdPO_4$ (denoted as Fe–Gd/HCS) (Scheme 1) were prepared to explore the size effect. Then systematic experiments were carried out to reveal the size effect of Fe–Gd/HCS nanoparticles on the interactions and cytotoxicity with cells *in vitro* by bio-TEM, CLSM, CCK-8 assay, and flow cytometry. The size-dependent increase of the number of internalized Fe–Gd/HCS was clearly observed. And the *in vivo* size effect of Fe–Gd/HCS was visualized by taking advantage of the embedded MRI nanoagents (γ-Fe_2O_3 and $GdPO_4$). On the other hand, a decrease of signal intensity of the liver in T_2-weighted images was observed with the smallest size of 100 nm, exhibiting the most significant decrease in negative contrast at 0.25 h. This result suggested that the smallest size of Fe–Gd/HCS (~100 nm) can clearly distinguish the liver, overwhelming to the other sizes (~200 nm, ~300 nm). Our proof-of-principle studies using Fe–Gd/HCS-S as the theranostic agent preliminarily presented its capability for potential multi-modal imaging and therapy.

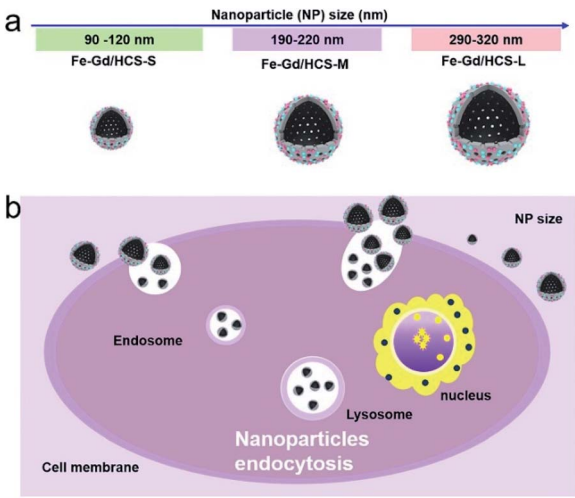

Scheme 1 (a) The schematic diagram of Fe–Gd/HCS with size vary from 100 to 320 nm and (b) the size-effect endocytosis of Fe–Gd/HCS nanoparticles.

Results and discussion

Preparing and tuning the size of Fe–Gd/HCS

Resorcinol formaldehyde (RF) coated SiO_2 (SiO_2@RF) core–shell nanoparticles were prepared by a classic two-step Stöber method, which was then post-synthetically functionalized with Wells–Dawson-like heterometallic clusters $\{Fe_6Gd_6P_6\}$,[37–39] giving SiO_2@RF/$\{Fe_6Gd_6P_6\}$. Carbonization and selective etching of the SiO_2 core resulted in the isolation of hollow carbon nanospheres on which γ-Fe_2O_3 and $GdPO_4$ stoichiometrically decomposed from $\{Fe_6Gd_6P_6\}$ were embedded (named Fe–Gd/HCS). Tuning the particle size was simply achieved by changing the EtOH volume from 25 to 35 and to 50 mL in the two-step Stöber process. As shown in Fig. 1, scanning electron microscopy (SEM) images confirmed their uniform spherical morphologies with the particle size varying from ~300 nm to ~200 nm and ~100 nm. Although further increasing amount of EtOH could lead to a constant decrease of particle size down to ~60 nm, large scale aggregation and adhesion of nanoparticles were observed. This phenomenon was not conducive to the application of nanoparticles for the following bio-evaluation (Fig. S1†). Hereafter, they were named Fe–Gd/HCS-L, Fe–Gd/HCS-M and Fe–Gd/HCS-S, respectively. Transmission electron microscopy (TEM) images confirmed their hollow structures with a cavity diameter/shell thickness of 180/70, 120/35 and 80/10 nm for Fe–Gd/HCS-L, Fe–Gd/HCS-M and Fe–Gd/HCS-S, respectively (Fig. 1 and S2†). The N_2 sorption isotherms showed a gradually enlarged hysteresis loop with the decrease of nanoparticle size. And the BET surface area/pore diameter of Fe–Gd/HCS-S, Fe–Gd/HCS-M and Fe–Gd/HCS-L were 539/4.0, 432/4.0 and 413/4.0 (m^2 g^{-1} nm^{-1}), respectively (Fig. S3 and S4†). The enhanced hysteresis

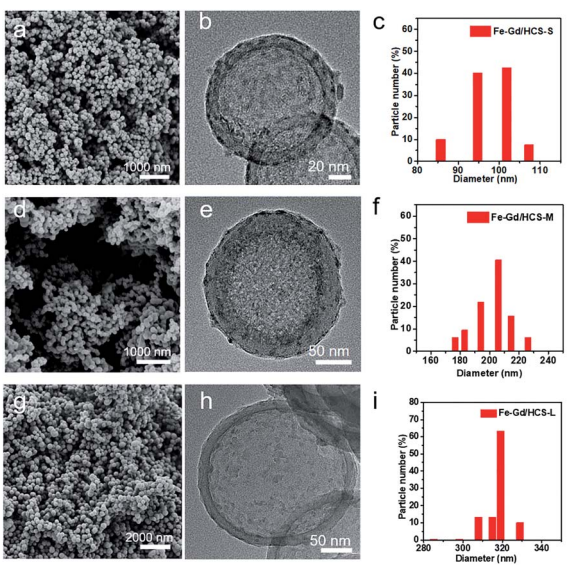

Fig. 1 SEM and TEM images of the as-synthesized Fe–Gd/HCS nanoparticles: (a and b) Fe–Gd/HCS-S, (d and e) Fe–Gd/HCS-M, and (g and h) Fe–Gd/HCS-L. (Right) Corresponding particle size histograms obtained by statistical analysis of over 150 particles: (c) Fe–Gd/HCS-S, (f) Fe–Gd/HCS-M, and (i) Fe–Gd/HCS-L.

loop could be ascribed to the increased curvature of the hollow structure and the connectivity of mesopores. According to LaMer nucleation theory, increasing EtOH amount contributed to the burst nucleation of SiO_2 and meanwhile limited its diffusion and growth, resulting in a small core for a large curvature of HCSs. Then coating RF on the core is governed by the Kelvin equation, in which the larger the curvature of SiO_2, the more difficult it is to coat RF as it requires a higher concentration of RF in the liquid phase. In this context, the coating-available RF was insufficient, which finally resulted in a thin thickness and the opening of pores at both ends of carbon shell. Irrespective of the curvature and shell thickness, the evaporation-induced-sorption of an equal amount of $\{Fe_6Gd_6P_6\}$ promoted homogeneous dispersion of stoichiometric γ-Fe_2O_3 and $GdPO_4$ as well as similar sizes and crystalline states, which were characterized by high-angle annular dark-field scanning transmission electron microscopy (HAADF-STEM), EDS line scanning, high-resolution TEM and powder X-ray diffraction analyses (Figure S5–S6†).

In vitro and *in vivo* evaluation of the size effect

Hydrodynamic diameters and surface charges were firstly examined by dynamic light scattering (DLS) and electrophoretic mobility (EM) measurement at room temperature (Fig. S7†). Despite the increase of hydrated nanospherical size, their considerable dispersity and negative charge characteristics were verified. Size-dependent cellular uptake was then investigated using a HeLa cell line, which was incubated with Fe–Gd/HCS (100 μg mL^{-1}) for 1 and 6 h respectively. As shown in Fig. 2 and S8,† bio-TEM images revealed an endo-lysosomal pathway, in which the Fe–Gd/HCS nanoparticles were internalized by endocytosis plausibly through a phagocytosis process. Then they are consequently delivered to endosomes, followed by final fusion with lysosomes. Size-dependent cellular uptake was clearly observed in the internalized nanoparticles following the order of Fe–Gd/HCS-S > Fe–Gd/HCS-M > Fe–Gd/HCS-L. In addition, as shown in the bright-field images, the cellular morphologies were retained well without obvious damage (Fig. S9†), indicating that Fe–Gd/HCS nanoparticles have no obvious cytotoxicity. Furthermore, the black nanoparticles slowly adhered to the cell membrane of HeLa cells after 1 h incubation. As the incubation time increased to 6 h, significant black nanoparticles were internalized into cytoplasm in accordance with the bio-TEM results.

Nanoparticles could cause autophagy and/or lysosomal dysfunction through the endo-lysosomal pathway, thus inducing cell necrosis and/or apoptosis.[40,41] The size-dependent cytotoxicity was therefore assessed by CCK-8 assay on HeLa, HepG2 and MCF-7 cell lines, respectively. For HeLa cells, as shown in Fig. 3a, the cell viability of HeLa cells incubated with Fe–Gd/HCS-S, Fe–Gd/HCS-M and Fe–Gd/HCS-L was above 80% even at concentrations up to 100 μg mL^{-1}, respectively. These

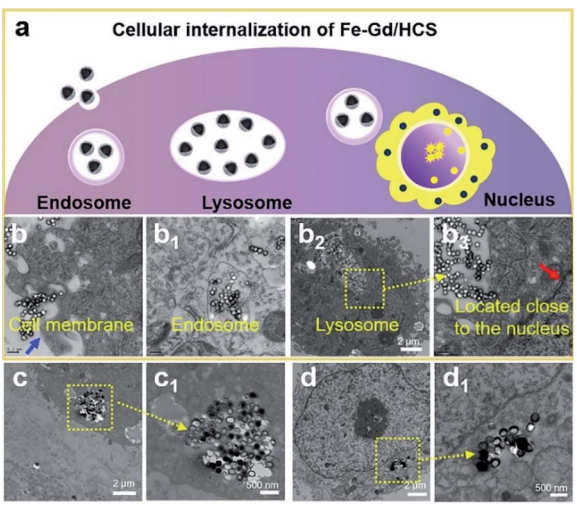

Fig. 2 (a) Schematic of the cellular internalization of Fe–Gd/HCS and (b) the corresponding bio-TEM images of the cell incubated with Fe–Gd/HCS-S (blue arrow indicates the cytoplasmic membrane, and the red arrow indicates the nuclear membrane, respectively): (b) Fe–Gd/HCS interacting with the cell membrane, (b_1) Fe–Gd/HCS carried inside the cell in vesicles, (b_2) Fe–Gd/HCS in the vesicles carried in the lysosome, and (b_3) Fe–Gd/HCS carried close to the nucleus. (c and d) Bio-TEM images of the HeLa cells incubated with Fe–Gd/HCS-M and Fe–Gd/HCS-L at the same concentration of 100 μg mL^{-1} after 6 h, respectively: (c) Fe–Gd/HCS-M and (d) Fe–Gd/HCS-L.

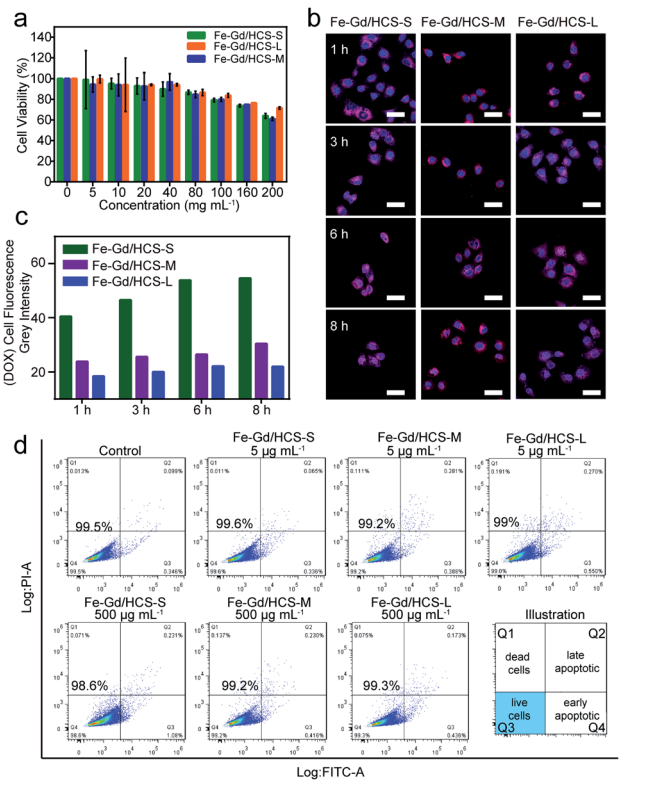

Fig. 3 (a) The viability of HeLa cells after incubation with Fe–Gd/HCS at different concentrations. (b) CLSM images of HeLa cells incubated with DOX@Fe–Gd/HCS for 1 h, 3 h, 6 h, and 8 h. Blue and red fluorescence represent DAPI and DOX in cells, respectively, and scale bar: 20 μm, and (c) the corresponding red fluorescence signal intensity. (d) Quantitative analysis of cell apoptosis by flow cytometry at 24 h after various treatments (Q1: dead cells, Q2: late apoptotic cells, Q3: early apoptotic cells, and Q4: live cells).

suggested little cytotoxicity for these three nanoparticles with different sizes. Quantitative analysis further exhibited no obvious apoptosis by flow cytometry after 24 hour incubation (Fig. 3d). These results indicated negligible cytotoxicity of Fe–Gd/HCS. Nevertheless, slight differences were observed between HeLa, MCF-7 and HepG2 cell lines (Fig. S10†), in which the Fe–Gd/HCS-L treated cells exhibited a slight increase in viability. This could be ascribed to the less internalized Fe–Gd/HCS-L nanoparticles as well as different sensitivities of cell lines.

Confocal laser scanning microscopy (CLSM) studies were further carried out to confirm the size-dependent cellular uptake (Fig. S11–S15 and Table S1†), in which blue-fluorescent DAPI was directly used for nuclear staining and red-fluorescent doxorubicin (DOX) loaded on Fe–Gd/HCS was used as a counterstaining probe. The cumulative DOX release behaviour of different Fe–Gd/HCS nanoparticles was firstly investigated in PBS solution (pH = 5.5), which revealed that the smaller size nanoparticles Fe–Gd/HCS-S could show higher values of DOX during the same time. Then, the CLSM experiments were performed with Fe–Gd/HCS at a safe concentration of 100 μg mL^{-1} based on the results of HeLa cells viability. After incubation for 1 h, blue fluorescence was readily observed in the nuclei of HeLa cells. And a weak signal of red fluorescence was observed in the cytoplasm. The analysis of the fluorescence intensity indicated gradual signal enhancement of red fluorescence as the incubation time increased from 1 to 8 h, revealing a cell-uptake process. At 1 h, the signal intensity in the case of Fe–Gd/HCS-S was approximately 1.69 and 2.20 times enhanced compared to that of Fe–Gd/HCS-M and Fe–Gd/HCS-L. Such observable enhancement remained steady with the increase of incubation time, demonstrating the size-dependent cellular uptake of Fe–Gd/HCS. This phenomenon matched well with previous studies on the effects of nanoparticle size on cellular uptake.[42]

The *in vivo* size effect of Fe–Gd/HCS was assessed by magnetic resonance imaging (MRI), because of the intrinsic magnetic properties of embedded γ-Fe_2O_3 and $GdPO_4$. *M–H* plots showed typical S-type curves without hysteresis loops but with a saturation magnetization (M_s) of 6.65, 7.21, and 4.31 emu g^{-1} at 2 T and 300 K for each Fe–Gd/HCS, indicating an overall superparamagnetic behavior (Fig. S16†). The r_1 and r_2 ($1/T_1$ and $1/T_2$) relaxivity values were then measured to be 3.7 and 175.1, and 3.3 and 164.7 mM^{-1} S^{-1} at 3.0 T (r.t.) for Fe–Gd/HCS-M and Fe–Gd/HCS-L, respectively (Fig. S17 and S18†). The r_1 and r_2 relaxivity values of Fe–Gd/HCS-S have already been calculated and reported in our previous paper.[36] It has been indicated that r_2 relaxivity mainly depends on the size, crystallinity and water-dispersity of T_2-contrast agents. The similarity of the particle size, crystallinity and amount of γ-Fe_2O_3 to each other can be expected due to the same post-synthesis process. Taking the size-dependent water-dispersity of nanoparticles into consideration, we tentatively ascribed the larger r_2 value of Fe–Gd/HCS-S to its conceivable dispersion stability in water. The calculated r_2/r_1 ratio is over 10 for each Fe–Gd/HCS, indicating a primarily T_2 contrast agent.[43,44] Consequently, Fe–Gd/HCS was respectively administrated by intravenous injection to normal and healthy female Balb/c mice. Considering the clearance mechanism of hard-nanomaterials,[45] *in vivo* MRI of the liver was performed at

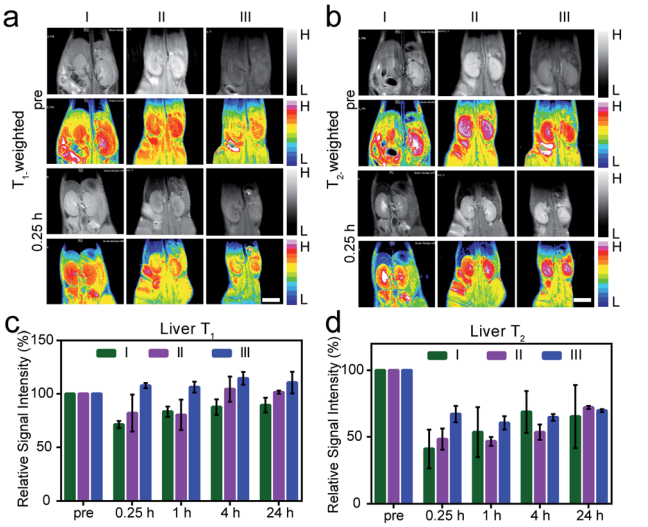

Fig. 4 (a and b) *In vivo* T_1-weighted and T_2-weighted MR images, and (c and d) the corresponding MR relative signal intensities of the liver of female BALB/c nude mice before and after tail intravenous injection of Fe–Gd/HCS after 0.25 h, 1 h, 4 h, and 24 h in a 7 T magnetic field at room temperature, and scale bar: 1 cm. ((I) Fe–Gd/HCS-S, (II) Fe–Gd/HCS-M, and (III) Fe–Gd/HCS-L, respectively).

different time intervals quantitatively. As indicated by the r_2/r_1 ratio, although the longitudinal (r_1) relaxivity value is comparable to that of some Gd-based MR contrast agents, the T_1-weighted images showed no obvious contrast enhancement though.[46,47] In contrast, an enhancement in T_2-weighted images was observed, in which Fe–Gd/HCS can clearly distinguish the liver from other tissues from darkening T_2-weighted images (Fig. 4 and S19–S21†). To quantify the enhancement, the regions of interest (ROIs) were selected on the T_1/T_2-weighted MR images of the liver, in which the signal-to-noise ratio was calculated according to a previously reported method.[48] Fe–Gd/HCS-S distinguished itself from the other two with a 59.0% decrease of the negative contrast at 0.25 h post-injection. The significant decrease could be ascribed to the active phagocytosis as well as the high r_2 relaxivity. Then the decrease of the negative contrast returns to 46.4% (at 1 h), 31.2% (at 4 h) and 34.8% (at 24 h) (Fig. 4c and d). The return of the signal indicated an easier sequestration of Fe–Gd/HCS-S *in vivo*. In addition, after another week of normal feeding, hematoxylin and eosin (H & E) stained tissue studies were carried out on the liver, spleen, kidney, heart and lung, which showed no obvious organ damage (Fig. 5).

In vivo therapeutic evaluation

The above *in vitro* and *in vivo* evaluation screen out of Fe–Gd/HCS-S and so the antitumor drug DOX loaded Fe–Gd/HCS (denoted as DOX@Fe–Gd/HCS-S) was therapeutically evaluated based on a HeLa cell xenografted mouse model (Fig. S22†). The tumor-bearing nude mice were randomly divided into two groups and treated with the following: PBS (control) and DOX@Fe–Gd/HCS-S. During a 16 d treatment period, there is no noticeable bodyweight loss. However, it was observed that the tumor volumes in the PBS-treated group increased gradually

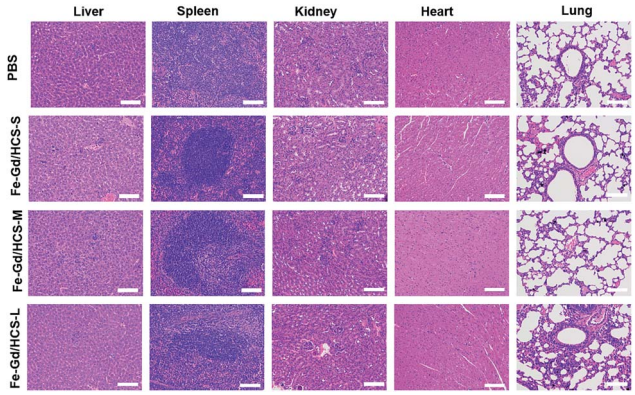

Fig. 5 Hematoxylin and eosin (H & E) images of the major organs collected from mice treated with PBS, and Fe–Gd/HCS-S, Fe–Gd/HCS-M, and Fe–Gd/HCS-L, and scale bar: 100 μm.

and reached to be 3.98-fold on day 16 (Fig. S23†). In contrast, treatment with DOX@Fe–Gd/HCS-S not only inhibited the tumor growth but also reduced the volume by 30.12% as compared with the size before treatment, indicating the availability of Fe–Gd/HCS-S for drug delivery (Fig. S24†). In addition, besides the above verified MRI performance, we also performed photoacoustic imaging (PAI) on the xenografted tumor by taking advantage of the photothermal conversion properties of Fe–Gd/HCS (Fig. S25†).[36] The PA signals in the tumor site were recorded at pre-injection, and 0.25, 1, 4, and 24 h post-injection. The PA signals showed an approximately 9.4-fold enhancement at 0.25 h post-injection compared to that of the tumor regions before the injection, suggesting the DOX@Fe–Gd/HCS-S was a novel candidate available for multi-modal imaging (Fig. S26†).

Conclusions

We have successfully achieved the isolation of hollow carbon nanospheres embedded with stoichiometric γ-Fe_2O_3 and $GdPO_4$ (Fe–Gd/HCS). Given its well-defined structure with tunable nanospherical size, our *in vitro* evaluation revealed that Fe–Gd/HCS could be internalized. And the cellular uptake amount is inversely proportional to the particle size. Despite the size-dependent endocytosis, there was no significant size-dependent cytotoxicity, revealing that the extracellular Fe–Gd/HCS could be intracellularly transported and degraded at the tested level. Furthermore, *in vivo* MRI studies demonstrated that Fe–Gd/HCS can distinguish the liver from other tissues, in which the smallest particle size was superior to Fe–Gd/HCS-M and Fe–Gd/HCS-L due to the size effect in our study. Our proof-of-principle studies using Fe–Gd/HCS as the theranostic agent preliminarily presented its capability for potential multi-modal imaging and therapy.

Experimental section

Materials and characterization

Chemicals. Tetraethyl orthosilicate (TEOS), resorcinol, formaldehyde solution (37 wt%), and concentrated ammonia solution (28 wt%) were of analytical grade and purchased from Shanghai Chemical Corp. $Fe(NO_3)_3 \cdot 9H_2O$, Gd_2O_3, pivalic acid, phenylphosphonic acid, acetonitrile (MeCN), triethylamine, sodium hydroxide (NaOH), ethanol (EtOH), doxorubicin hydrochloride (DOX), Dulbecco minimum essential medium (DMEM) solution, and 4′,6-diamidino-2-phenylindole (DAPI) were purchased from Aladdin. All chemicals were used as received without any further purification. Deionized water was used for all experiments.

Characterization. Powder X-ray diffraction data were recorded on a Bruker D8 Advance diffractometer at 40 kV and 40 mA with Cu-Kα radiation ($\lambda = 1.5406$ Å). Scanning electron microscopy (SEM) images were taken on a field emission scanning electron microscope (FE-SEM, Ultra55, ZEISS). TEM measurements were conducted on a JEM-2100 microscope (JEOL, Japan) operated at 200 kV. High-resolution TEM (HRTEM) was carried out on a FEI Tecnai F20 microscope. N_2 sorption at 77 K was measured on an ASAP 2020 gas adsorption apparatus (Micromeritics). Confocal images of cells were recorded with an Olympus FV1000 laser scanning confocal microscope and a 60× oil-immersion objective lens. The magnetic measurement was carried out on an MPMS superconducting quantum interference device (SQUID) VSM magnetometer equipped with a 7 T magnet. The magnetization isotherm was collected at 300 K between −2 and 2 T. The T_1-and T_2-weighted MR imaging experiments *in vitro* were performed on a Siemens Prisma 3.0 T MR scanner (Erlangen, Germany) with a gradient strength of up to 80 mT m^{-1}. *In vivo* T_1- and T_2-weighted MRI experiments were performed on a 7.0 T Bruker small animal MRI equipment. All the ultrasound (US) and photoacoustic (PA) images were obtained by using a Vevo LAZR photoacoustic imaging system (High resolution pre-clinical photoacoustic imaging system, FujiFilm Visualsonics Inc., USA).

Sample preparation

Synthesis of core–shell SiO_2@RF (resorcinol–formaldehyde). Monodisperse core–shell SiO_2@RF spheres were prepared by a modified Stöber coating method. Generally, 0.85 mL of TEOS mixed with 30 mL of ethanol were added to a solution containing ethanol (20 mL), deionized water (3 mL) and aqueous ammonia solution (2 mL) under stirring. After 1 h, 0.2 g of resorcinol and 0.28 mL of formaldehyde solution were added, respectively. The solution was stirred for 24 h at room temperature, and then transferred to a 100 mL Teflon-lined stainless-steel autoclave, and hydrothermally treated for 24 h at 100 °C. After cooling down, the solid product SiO_2@RF (100 nm, which was denoted as SiO_2@RF-S) was obtained by washing and air-drying at 60 °C for several hours. 200 nm and 300 nm sized SiO_2@RF were prepared with different ethanol amounts (35 mL and 15 mL) under the same conditions respectively, which were denoted as SiO_2@RF-M and SiO_2@RF-L.

Synthesis of Fe–Gd/HCS. The heterometallic cluster $\{Fe_6Gd_6P_6\}$ was prepared according to the literature.[37–39] Then following the evaporation-induced-sorption method,[49] SiO_2@RF/$\{Fe_6Gd_6P_6\}$ was isolated. Typically, 6 mg of $\{Fe_6Gd_6P_6\}$ clusters were dissolved in 2 mL of ethanol. Then 20 mg of the SiO_2@RF composites obtained above were added with stirring

at room temperature until ethanol was fully evaporated. Fe–Gd/HCS was prepared by (i) the carbonization of SiO_2@RF/{$Fe_6Gd_6P_6$} under a high-purity nitrogen stream at 600 °C for 3 h with a temperature ramp of 3 °C min^{-1}, (ii) etching the SiO_2 core with 2 M NaOH for 6 h at 60 °C. The isolated Fe–Gd/HCS was washed with water several times until there were no detectable sodium ions in water.

Bio-TEM of Fe–Gd/HCS-treated HeLa cells. The cellular uptake of Fe–Gd/HCS by HeLa cells was observed with a TEM (JEOL-1230, JEOL). After incubation with 10 μg mL^{-1} Fe–Gd/HCS for 1 h and 6 h respectively, the HeLa cells were prefixed with 2.5% glutaraldehyde at 4 °C for 4 h. Then the cells were post-fixed with 1% osmium tetroxide at 4 °C for 1 h. Both fixation and post-fixation steps included final rinsing in ultra-pure water and then stained with 0.5% uranyl acetate at 4 °C. The cells were dehydrated through a series of ethyl alcohol concentrations (*i.e.*, 30%, 50%, 70%, 80%, 90%, 100%, and dry alcohol) for 10 min each. Then, the cells were treated with propylene oxide, followed by 1 : 1 propylene oxide : resin for 2 h. The cells were infiltrated in resin at 70 °C for 24 h and ultramicrotomy was conducted. Then, the samples were observed with a TEM at 80 kV.

Cell cytotoxicity. The cytotoxicity of Fe–Gd/HCS on HeLa cells was evaluated by a Cell Counting Kit-8 (CCK-8) assay. Cells were harvested by trypsinization and seeded into a 96-well cell culture plate with 1×10^4 per well and incubated for 24 h at 37 °C under 5% CO_2. Then the cells were co-cultured with 5, 10, 20, 40, 80, 100, 160 and 200 μg mL^{-1} of Fe–Gd/HCS for 4 h, respectively. The kit of CCK-8 was then (10 μL·per well) added to each well and incubated at 37 °C for 1.5 h. Enzyme dehydrogenase in living cells was oxidized with this kit to an orange carapace. The quality was assessed calorimetrically by using a multi-reader (TECAN, Infinite M200, Germany). The measurements were based on the absorbance values at 450 nm. The viability of the cell was then calculated by using the following eqn (1):

$$\text{Viability (\%)} = [\text{Abs}_{(\text{sample})} - \text{Abs}_{(\text{blank})}]/[\text{Abs}_{(\text{control})} - \text{Abs}_{(\text{blank})}] \times 100\% \quad (1)$$

Following the same procedure, the cell viability of Fe–Gd/HCS on HepG2 cells and MCF-7 cells was also evaluated. Herein, the two cells were co-cultured with 5, 10, 20, 40, and 80 μg mL^{-1} of Fe–Gd/HCS (Fe–Gd/HCS-S, Fe–Gd/HCS-M and Fe–Gd/HCS-L), respectively.

Drug loading. 15 mg of Fe–Gd/HCS was dispersed into 2 mL (1 mg mL^{-1}) of DOX solution. The mixture was stirred for about 12 h at room temperature under dark conditions. Then the DOX-loaded sample was collected by centrifugation and washed three times with PBS. The supernatant and washed solutions were collected and analyzed by using a UV-vis spectrophotometer. The loading capacity was calculated and the concentration of DOX in the collection solution was determined at its maximum absorbance of 488 nm. These steps were repeated for the DOX-loaded Fe–Gd/HCS until the DOX concentration of the solution is steady. The drug loading capacity (LC) was calculated by using the following eqn (2):

$$\text{LC}_{\text{DOX}}\ (\%) = (W_{\text{DOX}}/W_{\text{sample}}) \times 100\% \quad (2)$$

where W_{DOX} is the loaded weight of DOX and W_{sample} is the weight of the activated Fe–Gd/HCS sample.

Drug release behavior in solution. DOX@Fe–Gd/HCS (2 mg) was dispersed in 30 mL of PBS solution (pH 5.5). At every interval, the above solution was centrifuged, and the supernatant was measured by using a UV-vis-NIR absorption spectrometer. The release percentage of DOX was calculated from the absorption spectra of PBS using a standard curve of absorbance at different concentrations of DOX. The release percentage (RP, w/w%) was evaluated by using eqn (3):

$$\text{RP} = W_{\text{release DOX}}/W_{\text{DOX}} \times 100\% \quad (3)$$

where W_{DOX} is the loading weight of DOX and $W_{\text{released DOX}}$ is the mass of the released DOX in the supernatant.

Size-dependent cellular uptake by CLSM. HeLa cells (5×10^4) were seeded on 10 mm confocal glass-bottom dishes for 24 h. Then the cell culture medium is changed to fresh DMEM (Dulbecco Minimum Essential Medium) with DOX@Fe–Gd/HCS (100 μg mL^{-1}). After incubation at 37 °C for 1 h, the cells were rinsed three times with PBS, followed by fixing with Paraformaldehyde solution for 15 min at 4 °C. Then, the nuclei of the HeLa cells were stained with DAPI (1 μg mL^{-1}). Finally, the cells were washed with PBS solution twice. The stained cells were imaged using an Olympus FluoView FV1000 confocal microscope (ex/em: 488/580–680 nm for DOX and ex/em: 405/550–650 nm for DAPI). Following the same procedure, the HeLa cells were treated with DOX@Fe–Gd/HCS for different time periods (3 h, 6 h, and 8 h).

Flow cytometry analysis. For flow cytometry analysis, the cells were seeded in a 6-well cell culture plate at a density of 4×10^5 cells per dish and treated with Fe–Gd/HCS with different concentrations of 5 μg mL^{-1} and 500 μg mL^{-1}. After 24 h incubation, the cells in the dishes were digested with trypsin, followed by centrifugation (1000 rpm, 4 °C, and 5 min) and washing with PBS twice. Finally, the cells were suspended in 1× binding buffer (100 μL) and then Annexin V-FITC (5 μL) and PI staining solution (5 μL) were added for 10 min. Flow cytometry (Beckman Coulter, USA) was used to measure their fluorescence emission quantitatively. An empty cell without addition of Fe–Gd/HCS was used as a control.

In vitro MRI. For *in vitro* MR images and both T_1 and T_2 measurements, Fe–Gd/HCS was dispersed in deionized water at various gadolinium (iron) concentrations. They were compared to those of deionized water used as a control. T_1-weighted MR images were acquired using a conventional spin-echo sequence with the following parameters: TR = 12 000 ms and TI = 20, 40, 80, 160, 320, 640, 1280, and 2560 ms. T_2-weighted MR images were acquired using a Car–Purcell–Meiboom–Gill sequence (CPMG) with the following parameters: TR/TE = 10 000, TE = 12, 24, 48, 96, 192, 382 ms. The specific relaxivity values of r_1 and r_2 were calculated through the curve fitting of $1/T_1$ and $1/T_2$ (s^{-1}) *versus* the concentration of the composite (mmol L^{-1}).

In vivo MRI experiments. Female BALB/c mice were purchased from Shanghai Slac Laboratory Animal Co., Ltd. Animal

experiments were carried out according to the protocols approved by the Animal Care and Use Committee of Fudan University. A serial of sequential MRI images at varying time points (0, 0.25, 1, 4 and 24 h) were acquired by intravenously injecting Fe–Gd/HCS (10 mg Fe kg^{-1}) into the mice *via* the tail vein.

The signal-to-noise ratio (SNR) was calculated according to the equation: liver signal-to-noise ratio $SNR_{liver} = SI_{liver}/SD_{noise}$ (where SI stands for signal intensity and SD stands for standard deviation) and the average relative liver signal intensities of mice (SNR_{post}/SNR_{pre}) are plotted at different time points (pre, 0.25, 1, 4 and 24 h).

All mice were euthanized after performing MRI. Then the major organs were sectioned into slices and then subjected to standard hematoxylin and eosin (H & E) staining for histological analysis.

***In vivo* antitumor effect and PA imaging assay.** Mice bearing HeLa tumors were prepared by subcutaneous injecting of 2×10^6 HeLa cells into the back of the hind light leg of female athymic nude mice.

When the tumor volume reached 100 mm^3, tumor-bearing nude mice were randomly divided into two groups and treated with the following: PBS (control) and DOX@Fe–Gd/HCS-S. Body weights and tumor sizes were recorded every two days for 16 days after the corresponding treatments. The tumor volume was calculated by using eqn (4):

$$\text{Volume} = (\text{width}^2 \times \text{length})/2 \quad (4)$$

The tumor growth inhibition rate was determined according to formula (5):

$$\text{Inhibition } (\%) = (C - T)/C \times 100 \quad (5)$$

where T means the average tumor weight of each treated group and C expresses the average tumor weight of the control group.

The *in vitro* and *in vivo* PA imaging ability of Fe–Gd/HCS was measured using a commercial Vevo LAZR PA imaging system with an excitation of 808 nm. A series of PA images at varying time points (pre, 0.25 h, 1 h, 4 h, and 24 h) were acquired.

Ethical approval

All animal procedures were performed in accordance with the Guidelines for Care and Use of Laboratory Animals of Fudan University and approved by the Animal Ethics Committee of Fudan University.

Conflicts of interest

There are no conflicts to declare.

Acknowledgements

We gratefully acknowledge the financial support from the National Natural Science Foundation of China (No. 21971045) and National Key Technologies R&D Program of China (2017YFA0205103).

Notes and references

1 J. Zhang and C. M. Li, *Chem. Soc. Rev.*, 2012, **41**, 7016–7031.
2 S. M. Kim, M. Jeon, K. W. Kim, J. Park and I. S. Lee, *J. Am. Chem. Soc.*, 2013, **135**, 15714–15717.
3 H. Tian, J. H. Zhao, X. Y. Wang, L. Z. Wang, H. Liu, G. X. Wang, J. Huang, J. Liu and G. Q. Lu, *Natl. Sci. Rev.*, 2020, **7**, 1647–1655.
4 Z. H. Yu, N. Ji, J. Xiong, X. Y. Li, R. Zhang, L. D. Zhang and X. B. Lu, *Angew. Chem., Int. Ed. Engl.*, 2021, **60**, 2–10.
5 X. B. Xu, Z. C. Zhang and X. Wang, *Adv. Mater.*, 2015, **27**, 5365–5371.
6 W. Zhu, Z. Chen, Y. Pan, R. Y. Dai, Y. Wu, Z. B. Zhuang, D. S. Wang, Q. Peng, C. Chen and Y. D. Li, *Adv. Mater.*, 2019, **31**, 1800426.
7 G. D. Moon, J. B. Joo, M. Dahl, H. Jung and Y. Yin, *Adv. Funct. Mater.*, 2014, **24**, 848–856.
8 S. N. Tiruneh, B. K. Kang, H. W. Choi, S. B. Kwon, M. S. Kim and D. H. Yoon, *Small*, 2018, **14**, 1802933.
9 J. Y. Wang, Y. Cui and D. Wang, *Adv. Mater.*, 2019, **31**, 1801993.
10 Y. J. Fang, D. Y. Luan, S. Y. Gao and X. W. D. Lou, *Angew. Chem., Int. Ed. Engl.*, 2021, **60**, 2–19.
11 K. An and T. Hyeon, *Nano Today*, 2009, **4**, 359–373.
12 Y. Chen, P. F. Xu, M. Y. Wu, Q. S. Meng, H. R. Chen, Z. Shu, J. Wang, L. X. Zhang, Y. P. Li and J. L. Shi, *Adv. Mater.*, 2014, **26**, 4294–4301.
13 L. S. Lin, J. Song, H. H. Yang and X. Y. Chen, *Adv. Mater.*, 2018, **30**, 1704639.
14 J. M. Park, H. E. Choi, D. Kudaibergen, J. H. Kim and K. S. Kim, *Front. Chem.*, 2021, **9**, 699284.
15 X. J. Wang, J. Feng, Y. Bai, Q. Zhang and Y. D. Yin, *Chem. Rev.*, 2016, **116**, 10983–11060.
16 D. Wang, A. Eychmüller and Y. Sun, *ChemNanoMat*, 2020, **6**, 1419–1420.
17 L. M. Wang, Q. Sun, X. Wang, T. Wen, J. J. Yin, P. Y. Wang, R. Bai, X. Q. Zhang, L. H. Zhang, A. H. Lu and C. Y. Chen, *J. Am. Chem. Soc.*, 2015, **137**, 1947–1955.
18 P. F. Zhang, Z. A. Qiao and S. Dai, *Chem. Commun.*, 2015, **51**, 9246–9256.
19 Y. W. Qiu, D. D. Ding, W. J. Sun, Y. S. Feng, D. D. Huang, S. C. Li, S. S. Meng, Q. L. Zhao, L. J. Xue and H. M. Chen, *Nanoscale*, 2019, **11**, 16351–16361.
20 Y. Z. W. Weng, S. Y. Guan, L. Wang, X. Z. Qu and S. Y. Zhou, *J. Mater. Chem. B*, 2019, **7**, 1920–1925.
21 B. Janic, M. P. Bhuiyan, J. R. Ewing and M. M. Ali, *ACS Sens.*, 2016, **1**, 975–978.
22 X. J. Cui, S. X. Xu, X. Y. Wang and C. Y. Chen, *Carbon*, 2018, **138**, 436–450.
23 J. B. Strachan, B. P. Dyett, Z. Nasa, C. Valery and C. E. Conn, *J. Colloid Interface Sci.*, 2020, **576**, 241–251.
24 D. Chauhan, S. Sri, R. Kumar, A. K. Panda and P. R. Solanki, *Nanotechnology*, 2021, **32**, 355101.
25 N. Hao, L. Li and F. Tang, *Int. Mater. Rev.*, 2016, **62**, 57–77.
26 Y. N. Yang, M. Jambhrunkar, P. L. Abbaraju, M. H. Yu, M. Zhang and C. Z. Yu, *Adv. Healthcare Mater.*, 2017, **6**, 1700466.

27 D. V. Kladko, A. S. Falchevskaya, N. S. Serov and A. Y. Prilepskii, *Int. J. Mol. Sci.*, 2021, **22**, 5266.
28 Y. Liu, B. Workalemahu and X. Y. Jiang, *Small*, 2017, **13**, 1701815.
29 T. Lunnoo, J. Assawakhajornsak and T. Puangmali, *J. Phys. Chem. C*, 2019, **123**, 3801–3810.
30 C. He, Y. Hu, L. Yin, C. Tang and C. Yin, *Biomaterials*, 2010, **31**, 3657–3666.
31 T. Mizuhara, K. Saha, D. F. Moyano, C. S. Kim, B. Yan, Y. K. Kim and V. M. Rotello, *Angew. Chem., Int. Ed. Engl.*, 2015, **54**, 6567–6570.
32 L. Li, W. S. Xi, Q. Su, Y. Li, G. H. Yan, Y. Liu, H. Wang and A. Cao, *Small*, 2019, **15**, 1901687.
33 H. B. Na, I. C. Song and T. Hyeon, *Adv. Mater.*, 2009, **21**, 2133–2148.
34 D. Ni, W. Bu, E. B. Ehlerding, W. Cai and J. Shi, *Chem. Soc. Rev.*, 2017, **46**, 7438–7468.
35 Q. Q. Zhang, P. Y. Wang, Y. Ling, X. M. Li, L. X. Xia, Y. T. Yang, X. F. Liu, F. Zhang and Y. M. Zhou, *Adv. Funct. Mater.*, 2017, **27**, 1605313.
36 H. Zhang, T. Z. Wu, Y. Chen, Q. Q. Zhang, Z. X. Chen, Y. Ling, Y. Jia, Y. T. Yang, X. F. Liu and Y. M. Zhou, *Nanoscale*, 2021, **13**, 10943–10952.
37 T. A. Zoan, N. P. Kuzmina, S. N. Frolovskaya, A. N. Rykov, N. D. Mitrofanova, S. I. Troyanov, A. P. Pisarevsky, L. I. Martynenko and Y. M. Korenev, *J. Alloys Compd.*, 1995, **225**, 396–399.
38 E. I. Tolis, M. Helliwell, S. Langley, J. Raftery and R. E. P. Winpenny, *Angew. Chem., Int. Ed.*, 2003, **42**, 3804–3808.
39 E. M. Pineda, F. Tuna, Y. Z. Zheng, S. J. Teat, R. E. Winpenny, J. Schnack and E. J. McInnes, *Inorg. Chem.*, 2014, **53**, 3032–3038.
40 J. Wang, Y. Yu, K. Lu, M. Yang, Y. Li, X. Zhou and Z. Sun, *Int. J. Nanomed.*, 2017, **12**, 809–825.
41 H. L. Zhou, X. Q. Gong, H. Y. Lin, H. M. Chen, D. T. Huang, D. Li, H. Shan and J. H. Gao, *J. Mater. Chem. B*, 2018, **6**, 8127–8136.
42 A. C. Wong and D. W. Wright, *Small*, 2016, **12**, 5592–5600.
43 F. Q. Hu, Q. J. Jia, Y. L. Li and M. Y. Gao, *Nanotechnology*, 2011, **22**, 245604.
44 M. Pernia Leal, S. Rivera-Fernandez, J. M. Franco, D. Pozo, J. M. de la Fuente and M. L. Garcia-Martin, *Nanoscale*, 2015, **7**, 2050–2059.
45 K. M. Tsoi, S. A. MacParland, X. Z. Ma, V. N. Spetzler, J. Echeverri, B. Ouyang, S. M. Fadel, E. A. Sykes, N. Goldaracena, J. M. Kaths, J. B. Conneely, B. A. Alman, M. Selzner, M. A. Ostrowski, O. A. Adeyi, A. Zilman, I. D. McGilvray and W. C. Chan, *Nat. Mater.*, 2016, **15**, 1212–1221.
46 T. Guo, Y. Lin, Z. Li, S. Chen, G. M. Huang, H. R. Lin, J. Wang, G. Liu and H. H. Yang, *Nanoscale*, 2017, **9**, 56–61.
47 G. M. Huang, K. L. Zhang, S. Chen, S. H. Li, L. L. Wang, L. P. Wang, R. Liu, J. Gao and H. H. Yang, *J. Mater. Chem. B*, 2017, **5**, 3629–3633.
48 J. Huang, L. H. Bu, K. Chen, Z. Cheng, X. G. Li and X. Y. Chen, *ACS Nano*, 2010, **4**, 7151–7170.
49 Q. Q. Zhang, P. Y. Wang, X. M. Li, Y. T. Yang, X. F. Liu, F. Zhang, Y. Ling and Y. M. Zhou, *J. Mater. Chem. B*, 2017, **5**, 3765–3770.